Solid-State Source of Subcycle Pulses in the Midinfrared

E. A. Stepanov, A. A. Lanin, A. A. Voronin, A. B. Fedotov, and A. M. Zheltikov

Phys. Rev. Lett. **117**, 043901 — Published 21 July 2016

DOI: 10.1103/PhysRevLett.117.043901

A solid-state source of subcycle pulses in the mid-infrared

E.A. Stepanov,[1,2] A.A. Lanin,[1,2] A.A. Voronin,[1,2]
A.B. Fedotov,[1,2] and A.M. Zheltikov[1,2,3,*]

[1]Physics Department, International Laser Center, M. V. Lomonosov Moscow State University, Moscow 119992, Russia

[2]Russian Quantum Center, 143025 Skolkovo, Moscow Region, Russia

[3]Department of Physics and Astronomy, Texas A&M University, 77843 College Station TX, USA

*Corresponding author: zheltikov@physics.msu.ru

We demonstrate a robust, all-solid-state approach for the generation of microjoule subcycle pulses in the mid-infrared through a cascade of carefully optimized parametric-amplification, difference-frequency-generation, spectral-broadening, and chirp-compensation stages. This method of subcycle waveform generation becomes possible due to an unusual, ionization-assisted solid-state pulse self-compression dynamics, where highly efficient spectral broadening is enabled by ultrabroadband four-wave parametric amplification phase-matched near the zero-group-velocity wavelength of the material.

Rapidly progressing photonic technologies offer an unprecedented control over optical field waveforms, enabling the generation of extremely brief flashes of electromagnetic radiation with accurately controlled shape, spectrum, and phase [1, 2]. At the forefront of the ongoing quest for ultrashort optical probes that would be capable of resolving extremely fast processes in gas-phase [3] and solid-state [4, 5] systems, technologies allowing the generation of electromagnetic lightwaves with temporal envelopes shorter than the field cycle have been developed [6–10], paving the ways toward an ultimate time resolution in electron-dynamic studies and subcycle precision in lightwave sculpting.

Subcycle field waveform generation has been demonstrated for the visible, near-infrared, terahertz, and x-ray ranges [7, 9]. In the mid-infrared region, on the other hand, subcycle field waveform generation has been only possible through a two-color filamentation

of ultrashort laser pulses [11]. In this regime, subcycle waveforms in the mid-infrared are generated as a part of conical emission, giving rise to ring-shaped beam profiles [12]. Moreover, multiple filamentation [13, 14] makes it difficult to scale this technology of subcycle waveform generation to higher peak powers, limiting the energy of subcycle mid-infrared pulses well below the microjoule level. Robust, solid-state sources capable of delivering power-scalable subcycle mid-infrared pulses in the fundamental spatial mode would serve to advance new schemes of high-harmonic generation using ultrashort mid-infrared driver pulses [15], which offer much promise for enhanced keV x-ray generation, as well as for a breakthrough into a zeptosecond range of pulse widths. Moreover, such a source would help to sculpt optimal field waveforms for the maximum energy of high-order harmonics, where a fraction of the mid-infrared field cycle would be necessary to provide the maximum energy of recolliding electrons [16,17], as well as to understand the fundamental quantum physics behind unusual nonlinear-optical properties of materials in the mid-infrared [18–20].

In this work, we fill the existing gap in subcycle lightwave electronics by demonstrating a robust, all-solid-state approach for the generation of microjoule subcycle pulses in the mid-infrared. In our experiments, multicycle mid-infrared pulses produced as a result of difference-frequency mixing of the signal and idler output of Ti: sapphire-pumped optical parametric amplifier are compressed to subcycle pulse widths by means of spectral broadening and subsequent chirp compensation in carefully optimized solid-state components.

In the absence of sufficiently broadband gain media in the mid-infrared, generation of femtosecond pulses in this important spectral region is largely based on optical parametric amplification (OPA) of mid-infrared pulses produced via difference-frequency generation (DFG). This technology has been recently shown to enable the generation of ultrashort mid-IR pulses at the subterawatt level of peak powers [21, 22], high-average-power sub-two-cycle mid-IR pulses at high repetition rates [23], as well as microjoule mid-IR waveforms compressible to few-cycle [24] and sub-two-cycle [25] pulse widths. However, with the OPA gain band limited by phase and group-index mismatch, generation of subcycle mid-IR pulses by means of this technology has never been possible.

Our experimental approach combines a wavelength-tunable OPA source of ultrashort, still multicycle mid-IR pulses with a carefully optimized scheme of nonlinear-optical transformation of the mid-IR OPA output, involving both spectral broadening and pulse self-compression, followed by additional pulse compression through residual chirp compensation.

Although the mid-IR OPA source, used at the first stage of this scheme, largely follows the standard OPA strategy, it has been modified in several ways, as explained in detail in the Supplemental Material (SM) [26], in order to minimize the group delay of pump, signal, and idler waves, which tend to have a detrimental effect on the pulse width and the phase of the mid-IR OPA output, without sacrificing too much of the mid-IR output energy and peak power.

To this end, optical parametric amplification was performed using two BBO crystals placed in sequence and pumped by a 62-fs, 825-nm, 1-kHz amplified Ti: sapphire-laser output (Fig. 1a in SM [26]). The signal and idler pulses delivered by the second BBO crystal are used to produce a wavelength-tunable field in the mid-IR through difference-frequency generation (DFG) in a 1-mm-thick $AgGaS_2$ (AGS) crystal. The wavelength tunability of the mid-IR DFG output is central to our scheme of subcycle pulse generation as the highest efficiency of spectral broadening is achieved by carefully adjusting the spectrum of an ultrashort mid-IR DFG output relative to the dispersion profile of the nonlinear element providing spectral broadening. Temporal and spectral characterization of mid-IR pulses was performed by cross-correlation frequency-resolved optical gating (XFROG) using four-wave mixing (FWM) in a gas [11, 36] (see SM [26] for details).

The central wavelength of the DFG output in our experiments can be tuned, by frequency-tuning the signal and idler pulses, within the range of wavelengths from approximately 2.7 to 14 μm. Our main focus here is, however, on a much narrow spectral range, where efficient compression to subcycle pulse widths can be achieved. This purpose is best served by a 150-μJ, 58-fs signal pulse centered at 1.48 μm and a 100-μJ, 61-fs signal wave with a central wavelength of 1.89 μm (Figs. 2d, 2e in SM [26]). The spectrally filtered mid-IR output produced as a result of DFG has a central wavelength of 6.8 μm, an energy of 5.0 μJ, and a pulse width of about 140 fs. This beam is collimated by a pair of off-axis 10-cm-focal-length parabolic mirrors before it enters a GaAs plate, where the mid-IR field undergoes spectral and temporal nonlinear-optical transformations leading to spectral broadening and changes in the pulse envelope. The regime of these nonlinear-optical transformations is highly sensitive to the relative arrangement of the spectrum of the mid-IR pulse and the dispersion profile of the material. Of particular interest for efficient spectral broadening and efficient pulse compression is the case when the spectrum of the field hits the point of zero group-velocity dispersion (GVD). In this situation (Fig. 1a), multiple cascaded four-wave mixing processes leading to a parametric energy transfer from the central part of the spectrum to

Stokes and anti-Stokes sidebands become phase-matched, dramatically enhancing spectral broadening.

In Fig. 1a, we plot the coherence length $l_c = \pi/|2\delta k|$, $\delta k = 2k_0 - k_s - k_a$, for a generic FWM process $2\omega_0 = \omega_s + \omega_a$, which transfers the energy from a mid-IR pump with a frequency ω_0 and wave vector $\mathbf{k}_0$ to Stokes and anti-Stokes sidebands with frequencies ω_s and ω_a and wave vectors $\mathbf{k}_s$ and $\mathbf{k}_a$, respectively. Calculations are performed for the dispersion of GaAs. The most striking feature of this map is that, within a narrow region centered at around the zero-GVD wavelength ($\lambda_z \approx 6.8$ μm for GaAs), an ultrabroadband phase matching is achieved for the $2\omega_0 = \omega_s + \omega_a$ FWM process, providing a physical mechanism for a dramatic enhancement of supercontinuum generation. Supercontinuum generation is indeed dramatically enhanced in our experiments when the mid-IR DFG output is tuned close to the zero-GVD wavelength of GaAs, exactly as shown in Fig. 1a. With a considerable fraction of the supercontinuum spectrum falling within the range of anomalous dispersion and with plasma effects drastically enhanced due to the λ^2 scaling of plasma refractivity, the temporal evolution of ultrabroadband field waveforms, emerging as a part of this dynamics, is very complicated and in many ways unusual as it involves strongly coupled nonlinear phenomena induced by ultrafast ionization and the Kerr-type optical nonlinearities of the solid-state material (Fig. 1b).

To understand this physical scenario, we resort to a numerical analysis based on the three-dimensional time-dependent generalized nonlinear Schrödinger equation (GNSE) [13, 14] for the amplitude of the mid-IR pulse propagating through a nonlinear medium (see SM [26] for details). The GNSE is solved jointly with the rate equation for the electron density, which includes photoionization and impact ionization. Such a physical model includes all the key physical effects pertinent to the nonlinear-optical evolution of ultrashort pulses in the experiments presented in this work, *viz*., material dispersion to all the orders, absorption, diffraction, spatial and temporal self-action effects due to the Kerr-type optical nonlinearity, including the higher order Kerr effect, self-steepening, as well as ionization-induced refraction and nonlinearities. When applied to the experiments presented here, this model accurately reproduces both the experimental temporal profiles and spectra of mid-IR field waveforms behind the GaAs plate retrieved from FWM XFROG traces (Figs. 2a, 2d). This agreement with all the available experimental data (Figs. 2b, 2c, 2e, 2f) verifies the predictive power of our model.

The decisive moments of the spectral--temporal evolution of the mid-IR field in the GaAs plate are illustrated in Figs. 3a – 3d. As the phase-matched FWM near the zero-GVD wavelength gives rise to enhanced spectral broadening, which is readily seen in the spectral–temporal maps in Fig. 3a, several unusual effects become apparent in the dynamics of the mid-IR pulse. Ordinarily, the trailing edge of the pulse, which carries the high-frequency part of the spectrum (see Fig. 3a), would be stretched by the normal dispersion of GaAs. However, the dynamics observed in Figs. 3a – 3d is strikingly different. Due to the λ^2 scaling of plasma refraction, ionization effects tend to play much more significant role in the dynamics of mid-IR pulses than they would play in the near-IR range. Ultrafast ionization of the solid by the mid-IR driver gives rise to a rapid buildup of the electron density $\rho(t)$, which translates into a steep ramp of plasma refractive index $\Delta n_{\mathrm{pl}} = \delta n_{\mathrm{pl}} + i\delta k_{\mathrm{pl}}$. The real part of Δn_{pl} contributes to the overall nonlinear, intensity dependent part of the refractive index $\delta n_{\mathrm{nl}} = \delta n_{\mathrm{K}} + \delta n_{\mathrm{pl}}$ (solid and dotted lines in Fig. 1b), where $\delta n_{\mathrm{K}} = n_2 I(t)$ is the change in the refractive index induced by the Kerr effect, with n_2 being the nonlinear refractive index. Both ionization-induced refraction and absorption, which is controlled by the imaginary part of Δn_{pl} (grey shading in Fig. 1b), rapidly build up toward the back of the pulse (see Fig. 1b), strongly attenuating the trailing edge of the pulse and enhancing the high-frequency wing of the spectrum (for z ranging from 4 to 5 mm in Fig. 3a). In an equivalent picture, this effect can be understood in terms of self-phase modulation within a pulse that evolves toward an asymmetric temporal profile with a steep trailing edge. Since the ultrafast ramp of electron density tends to shut the trailing edge of the pulse keeping the top of the pulse unaffected (Fig. 1b), the steeper trailing edge of the pulse gives rise to an enhanced generation of high-frequency components (Fig. 3a).

Ultrabroadband phase matching near the zero-GVD wavelength (Fig. 1a) couples these ionization-induced high-frequency components to the long-wavelength part of the spectrum through the $2\omega_0 = \omega_{\mathrm{s}} + \omega_{\mathrm{a}}$ FWM process, in which the ionization-induced high-frequency components serve as an ω_{a} seed, facilitating the generation of new ω_{s} frequency components, thus enhancing the long-wavelength wing of the spectrum ($z \approx 4 – 5$ mm in Fig. 3a) and increasing the overall supercontinuum bandwidth. Self-focusing also plays a noticeable role in the considered pulse self-compression scenario, as it partially suppresses diffraction-induced beam divergence, helping to keep the field intensity high within the entire beam path within the GaAs plate (Fig. 3d).

As the bandwidth of the mid-IR field waveform approaches an octave, which would correspond to a single-cycle pulse width in the case of a transform-limited pulse, an optical shock wave tends to build up on the trailing edge of the pulse. Because of its low intensity, the trailing edge of the pulse induces a smaller nonlinear change in the group index compared to the central, most intense part of the pulse, which gives rise to the largest change in the group index and, thus, propagates slower than the pulse edges. It is instructive to estimate the self-steepening of the trailing edge of the pulse occurring as a result of this process using an elementary theory of self-steepening, allowing a self-similar solution for a self-steepening pulse envelope [37]. In this approximation, the lag time of the peak of the pulse induced by pulse self-steepening for the parameters of our experiments is estimated as $\Delta\tau_s \approx 20$ fs (vertical dotted lines in Fig. 1b), providing a helpful quantitative measure of pulse self-steepening in our experiments and facilitating a better understanding of experimental pulse profiles in both experiments (solid line in Fig. 2b) and simulations (dash–dotted line in Fig. 2b).

The broadband mid-IR waveform behind the GaAs plate has a spectrum spanning, at 10% of its maximum, over more than an octave, from approximately 4.0 to 9.4 μm (Fig. 2c). The temporal profile of this waveform, retrieved from XFROG traces (Fig. 2a), has a short central peak with an FWHM pulse width of 29 fs and a prepulse (Fig. 2b), which rolls off to the $1/e$ level at –31 fs and which contains about 35% of the total energy of the mid-IR pulse. This waveform has a residual chirp, shown by the dashed line in Figs. 2b and 2c, which can be partially compensated by an anomalously dispersive material. Indeed, following chirp compensation in a 0.5-mm-thick BaF_2 plate, this pulse was compressed to an FWHM pulse width of 20 fs with prepulse suppression below 5% of the intensity of the central peak of the pulse (Fig. 2e). The energy within this suppressed prepulse was less than 10% of the total energy of the pulse. With the spectrum of the compressed mid-IR waveform centered at 6.8 μm (Fig. 2f), the 20-fs pulse width corresponds to less than 0.9 field cycles. The energy of the central, 20-fs peak of the pulse is estimated as 1 μJ, translating into a peak power of this waveform of about 50 MW. In the regime when the shortest, subcycle pulses were generated following additional chirp compensation in an anomalously dispersive material, an overall energy loss due to plasma absorption in GaAs does not exceed 13%.

To summarize, we have demonstrated a robust, all-solid-state approach for the generation of microjoule subcycle pulses in the mid-infrared through a cascade of carefully optimized parametric-amplification, difference-frequency-generation, spectral-broadening,

and chirp-compensation stages. The pulse self-compression scenario that takes place under the conditions of our experiments is in now way explained by soliton self-compression as it is dominated instead by strongly coupled nonlinear phenomena induced by ultrafast ionization and the Kerr-type optical nonlinearities of the solid-state material. The anomalous dispersion of GaAs does play a significant role under conditions of our experiments, but contributes to self-compression through mechanisms other than soliton self-compression. In pulse self-compression dynamics revealed in this work, anomalous dispersion helps provide ultrabroadband phase matching for FWM near the zero-GVD wavelength and reduces the temporal stretching of the leading edge of the pulse, which carries the long-wavelength part of the supercontinuum spectrum. This new scenario of solid-state pulse self-compression enables, as our experiments and simulations presented in this paper show, compression of mid-IR pulses to subcycle pulse widths.

This research was supported in part by the Russian Foundation for Basic Research (project nos. 14-29-07182, 15-32-20713, 14-02-00784 and 16-02-00843) and the Welch Foundation (Grant No. A-1801). Research into the nonlinear optics in the mid-infrared has been supported by the Russian Science Foundation (project no. 14-12-00772).

References

[1] E. Goulielmakis, V. S. Yakovlev, A. L. Cavalieri, M. Uiberacker, V. Pervak, A. Apolonski, R. Kienberger, U. Kleineberg, F. Krausz, Science **317,** 769 (2007).

[2] A. Wirth, M. Th. Hassan, I. Grguraš, J. Gagnon, A. Moulet, T. T. Luu, S. Pabst, R. Santra, Z. A. Alahmed, A. M. Azzeer, V. S. Yakovlev, V. Pervak, F. Krausz, E. Goulielmakis, Science **334**, 195, (2011).

[3] P.B. Corkum and F. Krausz, Nature Phys. **3,** 381 (2007).

[4] M. Schultze, E. M. Bothschafter, A. Sommer, S. Holzner, W. Schweinberger, M. Fiess, M. Hofstetter, R. Kienberger, V. Apalkov, V. S. Yakovlev, M. I. Stockman, and F. Krausz, Nature **493**, 75 (2013).

[5] F. Krausz and M. I. Stockman, Nature Photon. **8**, 205 (2014).

[6] M. Y. Shverdin, D. R. Walker, D. D. Yavuz, G. Y. Yin, and S. E. Harris, Phys. Rev. Lett. **94**, 033904 (2005).

[7] M. Th. Hassan, A. Wirth, I. Grguraš, A. Moulet, T. T. Luu, J. Gagnon, V. Pervak and E. Goulielmakis, Rev. Sci. Instrum. **83**, 111301 (2012).

[8] S.-W. Huang, G. Cirmi, J. Moses, K.-H. Hong, S. Bhardwaj, J. R. Birge, L.-J. Chen, E. Li, B. J. Eggleton, G. Cerullo, and F. X. Kärtner, Nature Photonics **5**, 475 (2011).

[9] C. Manzoni, O. D. Mücke, G. Cirmi, S. Fang, J. Moses, S.-W. Huang, K.-H. Hong, G. Cerullo and F. X. Kärtner, Laser Photonics Rev. **9**, 129 (2015).

[10] T. Balciunas, C. Fourcade-Dutin, G. Fan, T. Witting, A.A. Voronin, A.M. Zheltikov, F. Gerome, G.G. Paulus, A. Baltuska, and F. Benabid, Nature Commun. **6,** 6117 (2015).

[11] Y. Nomura, H. Shirai, K. Ishii, N. Tsurumachi, A. A. Voronin, A. M. Zheltikov, and T. Fuji, Opt. Express **20,** 24741 (2012).

[12] A.A. Voronin, Y. Nomura, H. Shirai, T. Fuji, and A.M. Zheltikov, Appl. Phys. B **117,** 611 (2014).

[13] A. Couairon and A. Mysyrowicz, Phys. Rep. **441,** 47 (2007).

[14] L. Berge, S. Skupin, R. Nuter, J. Kasparian and J.-P. Wolf, Rep. Prog. Phys. **70,** 1633 (2007).

[15] T. Popmintchev, M.-C. Chen, D. Popmintchev, P. Arpin, S. Brown, S. Alisauskas, G. Andriukaitis, T. Balciunas, O.D. Mücke, A. Pugzlys, A. Baltuska, B. Shim, S.E. Schrauth, A. Gaeta, C. Hernandez-Garcia, L. Plaja, A. Becker, A. Jaron-Becker, M.M. Murnane, and H.C. Kapteyn, Science **336,** 1287 (2012).

[16] R. Bartels, S. Backus, E. Zeek, L. Misoguti, G. Vdovin, I. P. Christov, M. M. Murnane, and H. C. Kapteyn, Nature **406,** 164 (2000).

[17] L. E. Chipperfield, J. S. Robinson, J. W. G. Tisch, and J. P. Marangos, Phys. Rev. Lett. **102,** 063003 (2009).

[18] P. Agostini and L. F. DiMauro, Contemp. Phys. **49,** 179 (2008).

[19] C.I. Blaga, F. Catoire, P. Colosimo, G.G. Paulus, H.G. Muller, P. Agostini, and L.F. DiMauro, Nature Phys. **5,** 335 (2008).

[20] E.E. Serebryannikov, and A. M. Zheltikov, Phys. Rev. Lett. **113**, 043901 (2014).

[21] G. Andriukaitis, T. Balčiūnas, S. Ališauskas, A. Pugžlys, A. Baltuška, T. Popmintchev, M.-C. Chen, M.M. Murnane, and H.C. Kapteyn, Opt. Lett. **36**, 2755 (2011).

[22] A.V. Mitrofanov, A.A. Voronin, D.A. Sidorov-Biryukov, A. Pugžlys, E.A. Stepanov, G. Andriukaitis, T. Flöry, S. Ališauskas, A.B. Fedotov, A. Baltuška, and A.M. Zheltikov, Scientific Reports **5**, 8368 (2015).

[23] I. Pupeza, D. Sánchez, J. Zhang, N. Lilienfein, M. Seidel, N. Karpowicz, T. Paasch-Colberg, I. Znakovskaya, M. Pescher, W. Schweinberger, V. Pervak, E. Fill,4, O. Pronin, Z.Wei, F. Krausz, A. Apolonski, and J. Biegert, Nature Photonics **9**, 721 (2015).

[24] M. Hemmer, M. Baudisch, A. Thai, A. Couairon, and J. Biegert, Opt. Express **21**, 28095 (2013).

[25] A. A. Lanin, A. A. Voronin, E. A. Stepanov, A. B. Fedotov, and A. M. Zheltikov, Opt. Lett. **39**, 6430 (2014).

[26] See Supplemental Material [url], which includes Refs. [27 – 35].

[27] L. V. Keldysh, Zh. Eksp. Teor. Fiz. **47,** 1945 (1964) [Sov. Phys. JETP **20,** 1307 (1965)].

[28] B.R. Bennett, R.A. Soref, J.A. del Alamo, IEEE Journal of Quantum Electronics, **26,** 113 (1990).

[29] W. G. Spitzer and J. M. Whelan, Phys. Rev. **114,** 59 (1959).

[30] P. B. Corkum, P. P. Ho, R. R. Alfano, and J. T. Manassah, Opt. Lett. **10**, 624 (1985).

[31] A.H. Chin, O.G. Calderón, and J. Kono, Phys. Rev. Lett. **86**, 3292 (2001).

[32] A. Couairon, L. Sudrie, M. Franco, B. Prade, and A. Mysyrowicz, Phys. Rev. B **71**, 125435 (2005).

[33] W. C. Hurlbut, Yun-Shik Lee, K. L. Vodopyanov, P. S. Kuo, and M. M. Fejer, Opt Lett. **32,** 668 (2007).

[34] H. H. Li, J. Phys. Chem. Ref. Data **9,** 161 (1980).

[35] T. Skauli, P. S. Kuo, K. L. Vodopyanov, T. J. Pinguet, O. Levi, L. A. Eyres, J. S. Harris, M. M. Fejer, B. Gerard, L. Becouarn, and E. Lallier, J. Appl. Phys., **94,** 6447 (2003).

[36] A. A. Lanin, A. A. Voronin, A. B. Fedotov, and A. M. Zheltikov, Scientific Reports **4,** (2014).

[37] Agrawal, G.P. *Nonlinear Fiber Optics*, 3rd Edition **(**Academic Press, San Diego, 2001).

Figure captions

Fig. 1. (a) The coherence length $l_c = \pi/|2\delta k|$ of the $2\omega_0 = \omega_s + \omega_a$ FWM process in GaAs as a function of the wavelengths $\lambda_s = 2\pi c/\omega_s$ and $\lambda_a = 2\pi c/\omega_a$. The central wavelength of the mid-IR DFG output is shown by the vertical dotted line. (b) The time profiles of the intensity-dependent change in the refractive index induced by the Kerr effect $\delta n_K = n_2 I(t)$ (dotted line) and the total nonlinear part of the refractive index $\delta n_{nl} = \delta n_{pl} + \delta n_K$. The absolute value of the imaginary part of the plasma correction to the refractive index, $|\delta k_{pl}|$, is shown by grey shading. The rose solid curve with rose shading shows the temporal profile of the mid-IR pulse at $z = 5$ mm. The blue dash–dotted line is the temporal envelope of the mid-IR pulse at $z = 0$. The lag time of the peak of the pulse induced by pulse self-steepening, $\Delta\tau_s$, is shown by the vertical dotted lines.

Fig. 2. (a, d) FWM FROG traces of the mid-IR pulse behind the GaAs plate (a) and following chirp compensation in the 0.5-mm BaF_2 plate (d). (b, e) Temporal envelopes (solid and dash–dotted lines) and phases (dashed and dotted lines) and (c, f) spectra (solid and dash–dotted lines) and spectral phases (dashed and dotted lines) retrieved from FWM FROG traces (solid and dashed lines) and simulated by numerically solving the GNSE (dotted and dash–dotted lines) for the mid-IR pulse behind the GaAs plate (b, c) and following chirp compensation in the 0.5-mm BaF_2 plate (e, f).

Fig. 3. Spectral, temporal, and spatial evolution of ultrashort mid-infrared pulses in the self-compression regime. (a) the Wigner spectrograms and temporal envelopes of the mid-IR pulse along its propagation path in the GaAs plate, (b) the longitudinal profile of the on-axis electron density induced by the mid-IR pulse in the GaAs plate, (c) the time evolution of the pulse integrated over the beam, and (d) the beam dynamics of the mid-IR pulse along its propagation path in the GaAs plate. The solid curve shows the evolution of the beam full width at half-maximum.

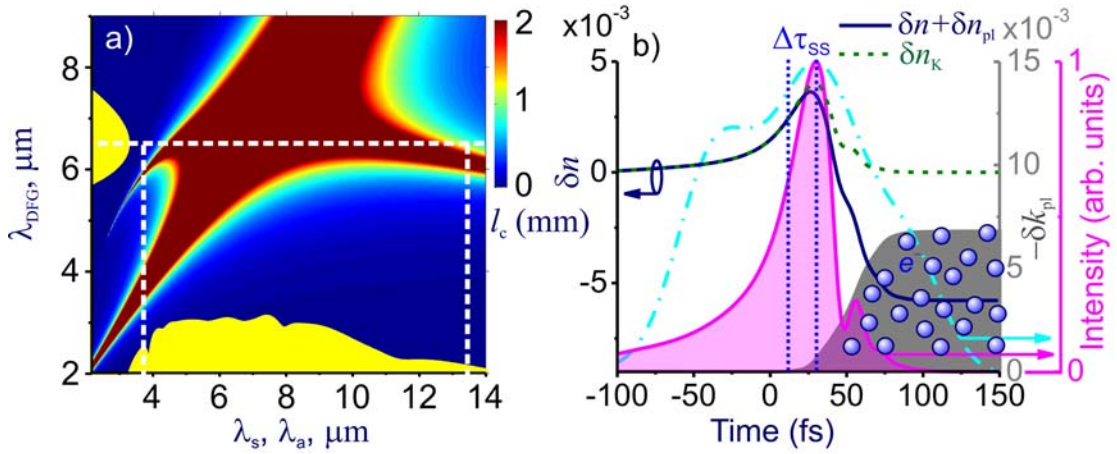

Fig. 1. (a) The coherence length $l_c = \pi/|2\delta k|$ of the $2\omega_0 = \omega_s + \omega_a$ FWM process in GaAs as a function of the wavelengths $\lambda_s = 2\pi c/\omega_s$ and $\lambda_a = 2\pi c/\omega_a$. The central wavelength of the mid-IR DFG output is shown by the vertical dotted line. (b) The time profiles of the intensity-dependent change in the refractive index induced by the Kerr effect $\delta n_K = n_2 I(t)$ (dotted line) and the total nonlinear part of the refractive index $\delta n_{nl} = \delta n_{pl} + \delta n_K$. The absolute value of the imaginary part of the plasma correction to the refractive index, $|\delta k_{pl}|$, is shown by grey shading. The rose solid curve with rose shading shows the temporal profile of the mid-IR pulse at $z = 5$ mm. The blue dash–dotted line is the temporal envelope of the mid-IR pulse at $z = 0$. The lag time of the peak of the pulse induced by pulse self-steepening, $\Delta\tau_s$, is shown by the vertical dotted lines.

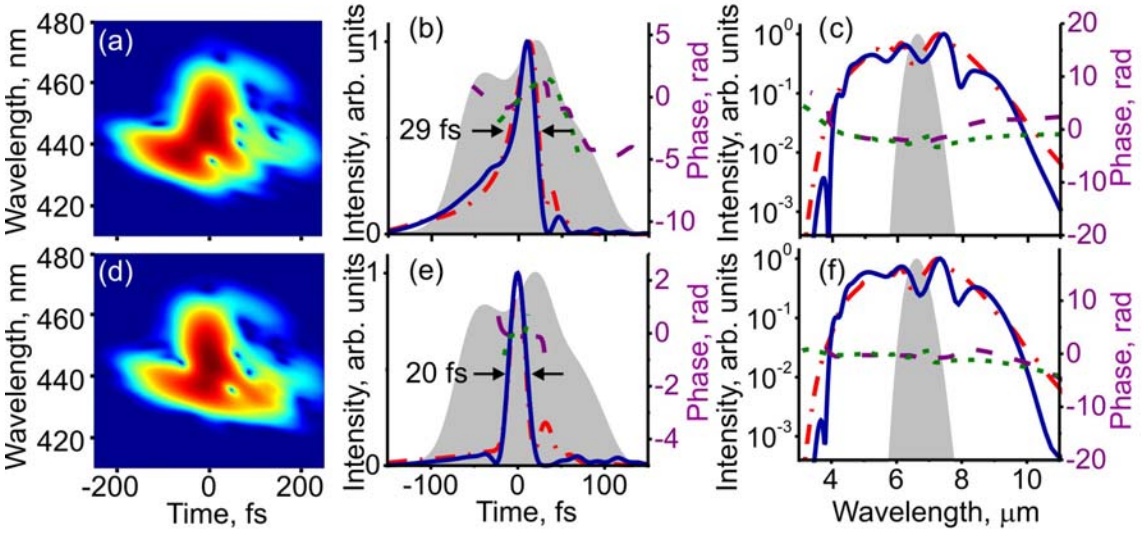

Fig. 2. (a, d) FWM FROG traces of the mid-IR pulse behind the GaAs plate (a) and following chirp compensation in the 0.5-mm BaF_2 plate (d). (b, e) Temporal envelopes (solid and dash–dotted lines) and phases (dashed and dotted lines) and (c, f) spectra (solid and dash–dotted lines) and spectral phases (dashed and dotted lines) retrieved from FWM FROG traces (solid and dashed lines) and simulated by numerically solving the GNSE (dotted and dash–dotted lines) for the mid-IR pulse behind the GaAs plate (b, c) and following chirp compensation in the 0.5-mm BaF_2 plate (e, f).

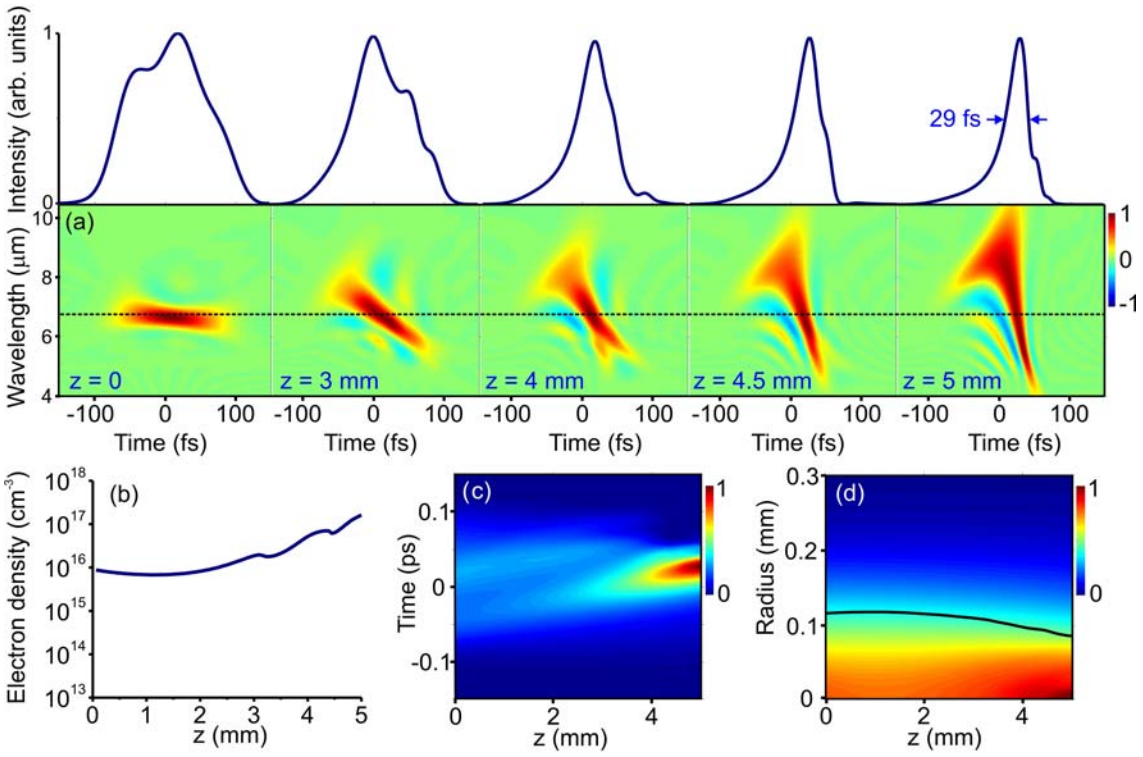

Fig. 3. Spectral, temporal, and spatial evolution of ultrashort mid-infrared pulses in the self-compression regime. (a) the Wigner spectrograms and temporal envelopes of the mid-IR pulse along its propagation path in the GaAs plate, (b) the longitudinal profile of the on-axis electron density induced by the mid-IR pulse in the GaAs plate, (c) the time evolution of the pulse integrated over the beam, and (d) the beam dynamics of the mid-IR pulse along its propagation path in the GaAs plate. The solid curve shows the evolution of the beam full width at half-maximum.